arXiv:1609.08260v1 [astro-ph.SR] 27 Sep 2016

On the role of repetitive magnetic reconnections in evolution of magnetic flux-ropes in solar corona

Sanjay Kumar, R. Bhattacharyya, and Bhuwan Joshi

Udaipur Solar Observatory, Physical Research Laboratory, Dewali, Bari Road, Udaipur-313001, India

P. K. Smolarkiewicz

European Centre for Medium-Range Weather Forecasts, Reading RG2 9AX, UK

Received _____; accepted _____

ABSTRACT

Parker's magnetostatic theorem extended to astrophysical magnetofluids with large magnetic Reynolds number supports ceaseless regeneration of current sheets and hence, spontaneous magnetic reconnections recurring in time. Consequently, a scenario is possible where the repeated reconnections provide an autonomous mechanism governing emergence of coherent structures in astrophysical magnetofluids. In this work, such a scenario is explored by performing numerical computations commensurate with the magnetostatic theorem. In particular, the computations explore the evolution of a flux-rope governed by repeated reconnections in a magnetic geometry resembling bipolar loops of solar corona. The revealed morphology of the evolution process including onset and ascent of the rope, reconnection locations and the associated topology of the magnetic field lines agrees with observations, and thus substantiates physical realisability of the advocated mechanism.

Subject headings: magnetic reconnection – magnetohydrodynamics (MHD) – Sun: corona – Sun: magnetic fields

1. Introduction

The astrophysical plasmas in general, and the solar corona in particular, are described by the non-diffusive limit of magnetohydrodynamics (MHD). The reason for such description is the large length scales and high temperatures, inherent to such plasmas which make the Lundquist number ($S = v_a L/\eta$, in usual notations) extremely high. For example, the Lundquist number for the solar corona, having a typical length scale $L \approx 10^7$m and magnetic diffusivity $\eta \approx 1\text{m}^2\text{s}^{-1}$ (Aschwanden 2004), is in the orders of 10^{13}. In such high-S plasmas, the Alfvén's theorem of flux-freezing (Priest 1982) is satisfied, thus predicting magnetic field lines (MFLs) to remain tied with fluid parcels during an evolution. With MFLs under coevolution with fluid parcels, a magnetic flux surface (MFS)—made by the loci of MFLs—once identified with a fluid surface, will maintain the identity throughout the evolution. As demonstrated by recent numerical simulations (Kumar et al. 2014, 2015b), such coevolution spontaneously develop current sheets (CSs); i.e., two dimensional surfaces of intense volume current density across which the MFLs flip sign. These simulations attribute the appearance of CSs to favorable contortions of MFSs, generic to the high-S magnetofluids dynamics. Noteworthy in the simulations is the development of a quasi steady state, approximately concurrent with the growing CSs. This is expected as the favorable contortions bring anti-parallel field lines in proximity and thereby increase local magnetic pressure which in turn, opposes further contortions. In the ideal scenario of $\eta = 0$, the quasi steady state corresponds to a steady state where magnetic field is discontinuous across a CS.

The above findings are in conformity with Parker's magnetostatic theorem (Parker 1972, 1988, 1994, 2012). The theorem states that the development of CSs is ubiquitous in an equilibrium magnetofluid with infinite electrical conductivity and complex magnetic topology. The development is due to a general failure of spatially continuous magnetic field

in achieving local equilibrium while preserving its topology. Generalization of the theorem to a magnetofluid undergoing topology-preserving evolution then naturally favors inevitable onset of CSs when the fluid relaxes toward a steady state. Here, the inevitability is due to unbalanced forces, which under flux-freezing have a constrained evolution that develop sharp gradients in the magnetic field (Parker 1994).

In presence of an otherwise negligible magnetic diffusivity, the CSs provide sites where the Lundquist number is locally reduced. The flux-freezing is destroyed and the locally diffusive magnetofluid undergoes magnetic reconnections (MRs) where magnetic energy is converted into energy of mass flow and heat. With reconnection, the CSs are dissipated, and MFLs being tied to fluid parcels are expunged from the reconnection sites along with the mass flow. These expunged field lines push onto other MFLs and, under favorable conditions, may lead to further reconnections. Importantly, a single reconnection can initiate consecutive secondary MRs, intermittent in space and time, which may shape up the dynamics of high-S magnetofluids. In a recent computational study (Kumar et al. 2015a) a scenario was explored, where repeated reconnections were identified as a cause for generating various magnetic structures, some duplicating magnetic antics of the Sun.

Toward realizing the above scenario in solar corona, we note that hard X-ray coronal sources are standardly accepted as signatures of magnetic reconnection in solar flares (Krucker et al. 2008). High resolution measurements show multiple peaks of non-thermal nature in flare's time profile, which suggest the corresponding energy releases and hence, the underlying reconnections, to be episodic (Joshi et al. 2013). Recent observations at multiple channels (hard X-ray and extreme ultraviolet) reveal intense localized brightening to occur below an ascending flux-rope (Kushwaha et al. 2015). The spatio-temporal correlation between intermittent energy release and ascent of an overlying flux-rope imply a causal connection between magnetic reconnections and the ascent (Cho et al. 2009; Cheng et al.

2011).

In the above perspective, this paper numerically demonstrates the evolution of a flux-rope in terms of its creation from initial bipolar field lines and continuous ascent, mediated via the common process of repeated spontaneous reconnections. The corresponding manifestations of magnetic topology—in likes of MRs occurring at a height, reconnections being localized below the rope and development of dips at the bottom part of the rope—are in general harmony with observations. This contrasts with the contemporary simulations of flux-ropes that judiciously precondition rope evolution—either by specifying preexisting twisted magnetic structures that emerge from below the photosphere (Fan 2001; Fan & Gibson 2003; Fan 2010, 2011; Chatterjee & Fan 2013; Fan 2016), or by forcing magnetic reconnections inside a sheared arcade with select (shearing and/or converging) initial flows (Ballegooijen & Martens 1989; Choe & Lee 1996; Amari et al. 1999, 2003; Aulanier et al. 2010; Xia et al. 2014). While the present work also explores MRs inside sheared arcades, the computations being in agreement with the magnetostatic theorem generate spontaneous reconnections which provide an autonomous mechanism to govern dynamics of any high-S magnetofluid. The novelty of this work is in its approach to establish creation and activation of a physically realizable flux-rope as a consequence of the autonomous mechanism. Introspectively, such a rope has the flavor of a self-organized state (Kusano et al. 1994).

To make numerical simulations agree with the theory of CS formation, the requirement is the satisfaction of flux-freezing to high fidelity between two successive MRs, while enabling local diffusion of MFLs co-located and concurrent with the developing CSs. These two requirements are achieved through the following numerical scheme. Viscous relaxation (Bhattacharyya et al. 2010; Kumar et al. 2014, 2015a,b) of a thermally homogeneous, incompressible magnetofluid with infinite electrical conductivity is employed to evolve

the fluid under the flux-freezing till CSs develop. To focus on the idea, the relevant Navier-Stokes MHD equations are

$$\frac{\partial \mathbf{v}}{\partial t} + (\mathbf{v}\cdot\nabla)\,\mathbf{v} = -\nabla p + (\nabla\times\mathbf{B})\times\mathbf{B} + \frac{\tau_a}{\tau_\nu}\nabla^2\mathbf{v} \quad , \tag{1}$$

$$\nabla\cdot\mathbf{v} = 0 \quad , \tag{2}$$

$$\frac{\partial \mathbf{B}}{\partial t} = \nabla\times(\mathbf{v}\times\mathbf{B}) \quad , \tag{3}$$

$$\nabla\cdot\mathbf{B} = 0 \quad , \tag{4}$$

in usual notations. The equations (1)-(4) are written in dimensionless form, with all variables normalized according to

$$\mathbf{B} \longrightarrow \frac{\mathbf{B}}{B_0} \quad , \tag{5}$$

$$\mathbf{v} \longrightarrow \frac{\mathbf{v}}{v_a} \quad , \tag{6}$$

$$L \longrightarrow \frac{L}{L_0} \quad , \tag{7}$$

$$t \longrightarrow \frac{t}{\tau_a} \quad , \tag{8}$$

$$p \longrightarrow \frac{p}{\rho {v_a}^2} \quad . \tag{9}$$

Here, the constants B_0 and L_0 are generally arbitrary, but can be fixed by the magnetic field strength and size of the system. Furthermore, $v_a \equiv B_0/\sqrt{4\pi\rho_0}$ is the Alfvén speed and ρ_0 is the constant mass density. The constants τ_a and τ_ν have dimensions of time, and represent Alfvén transit time ($\tau_a = L_0/v_a$) and viscous diffusion time scale ($\tau_\nu = L_0^2/\nu$) respectively, with ν being the kinematic viscosity. The pressure p satisfies the elliptic partial differential equation

$$\nabla^2\left(p + \frac{v^2}{2}\right) = \nabla\cdot\Big[(\nabla\times\mathbf{B})\times\mathbf{B} - (\nabla\times\mathbf{v})\times\mathbf{v}\Big] \tag{10}$$

generated by imposing the incompressibility (2) on the momentum transport equation (1); see (Bhattacharyya et al. 2010) for discussion. If released from an initial non-equilibrium

state, the above fluid evolves by converting magnetic energy into the energy of mass flow while the latter gets dissipated by viscosity. The terminal state is then expected to be static where the pressure gradient is balanced by the Lorentz force as MFLs cannot get diffused because of the flux-freezing. In simulations however, only a quasi-steady state is achieved, maintained by a partial balance of Lorentz force, pressure gradient and viscous drag; details of the energetics can be found in (Bhattacharyya et al. 2010; Kumar et al. 2014, 2015a,b). The CSs develop as the fluid relaxes to the terminal state.

As thickness of the developing CSs falls below the selected grid resolution, scales become under-resolved and numerical artifacts such as spurious oscillations are generated through employed numerical techniques. These under-resolved scales can be removed by utilizing an apt numerical diffusivity of non-oscillatory finite volume differencing. In literature, such calculations relying on the non-oscillatory numerical diffusivity are referred as Implicit Large Eddy Simulations (ILESs) (Grinstein 2007). The computations performed in this work are in the spirit of ILESs where simulated MRs, being intermittent in space and time, mimic physical reconnections in high-S fluids.

The rest of the paper is organized as follows. In section II we construct the initial magnetic field and discuss the numerical model. Section III is dedicated to results and discussions. In section IV, we summarize results and highlight important findings.

2. Initial magnetic field and numerical model

2.1. Initial magnetic field

To construct an initial magnetic field with field-line topology similar to coronal loops, we choose $\mathbf{B}(\mathbf{r}, t = 0)$ with the corresponding components

$$B_x = k_z \sin(k_x x) \exp\left(-\frac{k_z z}{s_0}\right) \quad , \tag{11}$$

$$B_y = \sqrt{{k_x}^2 - {k_z}^2} \sin(k_x x) \exp\left(-\frac{k_z z}{s_0}\right) \quad , \tag{12}$$

$$B_z = s_0 k_x \cos(k_x x) \exp\left(-\frac{k_z z}{s_0}\right) \quad , \tag{13}$$

defined in the positive half-space ($z \geq 0$) of a Cartesian domain, assumed periodic in x. The field is two dimensional as it only depends on x and z but not on y and hence, satisfy translational symmetry along y. The merit of this choice is that for $s_0 = 1$ $\mathbf{B}$ is reduced to a gauge-invariant form of the linear force-free field

$$\nabla \times \mathbf{B_{lf}} = \alpha_0 \mathbf{B_{lf}} \tag{14}$$

with the (constant) magnetic circulation per unit flux $\alpha_0 = \sqrt{{k_x}^2 - {k_z}^2}$ (Parker 2012), and the associated Lorentz force $(\nabla \times \mathbf{B}) \times \mathbf{B} := \mathbf{J} \times \mathbf{B} \equiv 0$. In the conducted simulation, the translational symmetry is crucial for an identification of detached magnetic structure with flux-rope. It helps to establish the reconnected field lines that generate a magnetic flux surface, while providing fundamental understanding necessary to explore activation of a three dimensional rope. Standardly, the solar corona is a low-β plasma with Lorenz force dominating all other forces, and the zero Lorentz force corresponding to a viable equilibrium (Priest 1982). With the initial $\mathbf{B}$ having congruent analytical form as $\mathbf{B}_{\rm lf}$ (Appendix A), the field lines are expected to resemble coronal loops. The shear angle between x-axis and the projection of an initial field line on the $z = 0$ plane,

$$\phi = \tan^{-1}\left(\frac{\sqrt{{k_x}^2 - {k_z}^2}}{k_z}\right) \quad , \tag{15}$$

is independent of s_0. If $k_x = k_z$, $\phi = 0$, and the field lines are tangential to y-constant planes. Generally, the Lorentz force exerted by the field defined in (11)-(13) is

$$(\mathbf{J}\times\mathbf{B})_x = \left[-k_x({k_x}^2 - {k_z}^2) + k_x s_0\left(s_0{k_x}^2 - \frac{{k_z}^2}{s_0}\right)\right]\sin^2(k_x x)\exp\left(-\frac{2k_z z}{s_0}\right)\ , \quad (16)$$

$$(\mathbf{J}\times\mathbf{B})_y = 0\ , \quad (17)$$

$$(\mathbf{J}\times\mathbf{B})_z = \left[\frac{k_z}{s_0}({k_x}^2 - {k_z}^2) - k_z\left(s_0{k_x}^2 - \frac{{k_z}^2}{s_0}\right)\right]\frac{\sin(2k_x x)}{2}\exp\left(-\frac{2k_z z}{s_0}\right)\ . \quad (18)$$

For all $s_0 \neq 1$, $\mathbf{J}\times\mathbf{B} \neq 0$, so the Lorentz force contributes to the viscous relaxation. To assure sheared field lines, we set $k_x = 1$ and $k_z = 0.9$ in the initial field (11)-(13). Furthermore, we set $s_0 = 6$, to optimize between computation cost and efficient development of dynamics leading to formation of CSs and their subsequent reconnections. This selection relied on the monotonous dependence of the maximal initial Lorentz force on s_0, Figure 1, and some auxiliary simulations (not reported here).

To aid further understanding, the following presents a detailed analysis of the initial magnetic field. For relevant depictions, hereafter, we set $x \in \{0, \pi\}$, because similar structures and dynamics are repeated in $x \in \{\pi, 2\pi\}$ due to the assumed periodicity. The MFLs for $s_0 = 6$ are shown in Figure 2 (a).[1] The arrows in colors red, green, and blue denote the axes x, y, and z respectively. The plotted MFLs are sheared loops with a straight polarity inversion line (PIL) located at $(x, z) = (\pi/2, 0)$. To highlight the shear, Figure 2 (b) illustrates projection of the field lines on $z = 0$ plane which are inclined to the x-axis at an angle $\phi \equiv \tan^{-1}(0.48) = 25.6°$. We keep ϕ fixed to this value for our simulations. Notably, the MFLs maintain translational symmetry along y since $\mathbf{B}$ is independent of y. For comparison, in panels a and b of Figure 3, we plot MFLs of the corresponding $\mathbf{B}_{\rm lf}$ (for $s_0 = 1$) and their projections on the $z = 0$ plane.

[1]The VAPOR visualization package (Clyne & Rast 2005) is used to integrate the field lines equations.

Coronal arcades—associated with flux rope formation—are generally believed to evolve from an initial quasi-equilibrium state, devoid of any major electric current density. An appropriate physical mechanism is then required to generate dynamics from the quasi-equilibrium. Such onset of dynamics can be achieved by a specialized photospheric flow used in (DeVore & Antiochos 2000), where fully compressive MHD simulations demonstrate generation of ropes through reconnections. The present computations, however, start from an initial non-equilibrium state with appreciable electric current density to make them harmonious with general framework of the viscous relaxation. For instance, the initial electric current density is roughly 15 times larger for the $\mathbf{B}$ in comparison to the $\mathbf{B}_{\rm lf}$ (cf. Figs. 2 and 3).

2.2. Numerical model

To solve the Navier-Stokes MHD equations (1)-(4), we utilize the well established magnetohydrodynamic numerical model EULAG-MHD (Smolarkiewicz & Charbonneau 2013), an extension of the hydrodynamic model EULAG predominantly used in atmospheric and climate research (Smolarkiewicz 2006; Prusa et al. 2008). Here we summarize only essential features of EULAG-MHD; the details are in Ref. (Smolarkiewicz & Charbonneau 2013) and references therein. The EULAG-MHD is based on the spatio-temporally second order accurate non-oscillatory forward-in-time multidimensional positive definite advection transport algorithm, MPDATA, (Smolarkiewicz 2006). Relevant to our simulations is MPDATA proven dissipative property, intermittent and adaptive to generation of under-resolved scales in field variables for a fixed grid resolution. With fixed grid resolution, a development of CSs inevitably generates under-resolved scales as a consequence of unbounded increase in the magnetic field gradient. The MPDATA then removes these under-resolved scales by producing locally effective residual dissipation of the second order,

sufficient to sustain monotonic nature of the solution. Being intermittent and adaptive, the residual dissipation facilitate the model to perform ILESs that mimics the action of explicit subgrid-scale turbulence models, whenever the concerned advective field is under-resolved (Margolin et al. 2006). Such ILESs performed with the model have already been successfully utilized to simulate regular solar cycles (Ghizaru et al. 2010), with the rotational torsional oscillations subsequently characterized and analyzed in (Beaudoin et al. 2013). The simulations reported continue relying on the effectiveness of ILES in regularizing the onset of MRs, concurrent and collocated with developing CSs (Kumar et al. 2013).

3. Simulation results

The simulations are performed on four differently sized grids—$128 \times 128 \times 256$, $64 \times 64 \times 128$, $40 \times 40 \times 80$ and $32 \times 32 \times 64$—resolving the computational domain $0, 2\pi \times 0, 2\pi \times 0, 8\pi$ (respectively in x, y, and z), all starting from a motionless state and initial field (11)-(13). The boundary conditions along x are periodic, and open in z. The y direction is analytically ignorable, because the governing equations (1)-(4) and the initial conditions assure all dependent variables invariant in y. However, for efficacy of the results postprocessing and their analysis with the VAPOR visualization package (Clyne & Rast 2005) we allow field variables to have all the three components while circumventing discrete differentiations in y. This makes field variables to have a translational symmetry along y, the maintenance of which can easily be verified from relevant plots presented in the paper. Moreover, for the case $32 \times 32 \times 64$ we have performed a fully 3D simulation, with no ignorable coordinate, and found results (not shown) to be in exact agreement with the corresponding 2.5D run.

In the conducted simulations, the dimensionless number $\tau_a/\tau_\nu \approx 10^{-5}$, and the effective S^{-1} is negligibly small apart from reconnections. The residual dissipation being

intermittent in time and space, a quantification of it is meaningful only in the spectral space where, in analogy to the eddy-viscosity of explicit subgrid-scale models for turbulent flows, it only acts on the shortest modes admissible on the grid (Domaradzki et al. 2003); in particular, in the vicinity of steep gradients in simulated fields. For parameter values relevant to solar corona (Aschwanden 2004), the ratio of Alfvén transit time to the viscous time scale $\tau_a/\tau_v \approx 10^{-4}$, which is one order of magnitude larger than that adopted in our computations. This, however, only affects the interval between two successive reconnections without an effect on the corresponding change in field line topology. Being incompressible, flow in our computations is volume preserving—an assumption also used in other works (Dahlburg et al. 1991; Aulanier et al. 2005). While compressibility is important for the thermodynamics of coronal loops (Ruderman & Roberts 2002), our focus is on elucidating changes in magnetic topology idealised with a thermally homogeneous magnetofluid. We select $\rho_0 = 1$ to have $\tau_a \approx 20s$, roughly corresponding to the coronal value with constants B_0 and L_0 set to 4 (amplitude of $\mathbf{B}$) and 8π (vertical length of the physical domain) respectively. The results for computation with resolutions $128 \times 128 \times 256$ are presented below.

To obtain overall understanding of the evolution, in Figure 4, we plot the time profile of normalized kinetic energy. The time profile shows four distinct phases which can approximately be divided into three overlapping intervals ranging from $t \in \{0s, 16s\}$, $t \in \{16s, 28s\}$, and $t > 28s$; separated by the vertical lines in the figure. The first phase corresponds to a rise in kinetic energy as the initial Lorentz force pushes the magnetofluid from rest. This rise is then arrested by viscous drag and the fluid settles down to a quasi-steady state which is characterized by an almost constant kinetic energy, representing the onset of the second phase. Also to be noted are the further rise and the following decay of kinetic energy which correspond to the third phase.

Figure 5 illustrates three sets of magnetic loops L1, L2, and L3, the evolution of which leads to a topologically distinct structure with field lines detached from the $z = 0$ surface. This detached structure resembles a magnetic flux-rope propagating along the y. For substantiation, in Figure 6 we plot the field lines in vicinity of the detached structure. The plot establishes the detached structure to be a flux-rope, made by helical field lines that are tangential to nested co-axial cylindrical surfaces. Away from the axis, the helices are more tightly wound. Importantly, the Figure 5 documents a sustained ascent of the flux-rope along the vertical while being always situated above the PIL. The latter is a general requirement for magnetic structures to represent solar prominences or filaments.

Toward an explanation for generation of the rope, notable is the implosion of MFLs with a simultaneous increase in their footpoint (the point at which MFLs intersect the $z = 0$ plane) separation as displayed in panel b of Figure 7. During the implosion, reconnection of footpoints is prohibited because only parallel MFLs are bundled together. With magnitude of the Lorentz force diminishing exponentially along the vertical, the implosion is non-uniform, being more effective at lower heights. The non-uniform implosion generates a void depleted of MFLs, leading to a local decrease in magnetic pressure on a y constant plane; cf. panel b of Figure 7. Consequently, parts of two complementary anti-parallel field lines, located on opposite sides of the PIL, are stretched along x and enter into this void (panel c). As a result, the gradient of $\mathbf{B}$ along x sharpens up, as confirmed by the Figure 8 that documents scaling of current density with resolution in the vicinity of the void. Consequently, magnetic reconnection takes place as the scales become under-resolved (panel d of Fig. 7). Such reconnections, repeated in time, are responsible for the origin of the rope. Crucial is the non-zero shear, or equivalently $B_y \neq 0$, which makes the reconnected field lines helical. In absence of shear, MFLs would have been closed disjoint curves tangential to y-constant planes—thus corresponding to a flux tube, but not a rope.

The projection of the rope on a y-constant plane corresponds to a magnetic island. In Figure 9 we plot evolution of the island at $t = 6s$ and $t = 8s$. Important is the appearance of an X-type magnetic null located below the island; illustrated in Figure 9 (a) by the symbol X. The MRs at the X-type neutral point increase number of MFLs constituting the island (panel b of Fig. 9). Also, the outflow generated by these repeated MRs at the X-point lifts the island center along the vertical. Notably, the above MRs are occurring while preserving the X-type null and no extended CS is developed, as documented by contours of current density in the Figure 7. The development of an extended CS by squashing a X-type null requires a favorable force missing in this period of evolution.

In Figure 10, we illustrate MFLs projected on a y-constant plane (panels a and b) and contours of current density (panels c and d) at instances $t = 16s$ and $t = 21s$, which correspond to the second phase of the evolution. From the figure, as reconnections at the X-type null continue, the magnetic pressure, below and above the two quadrants of the X-type null (denoted by $X1$ and $X2$ in panel a of the figure), increases. The increased magnetic pressure results in squashing of the X-type null and leads to formation of two Y-type nulls along with an extended CS (panels b and d). Importantly, the development of this extended CS is concurrent with the quasi-steady phase of the evolution $t \in \{16s, 28s\}$, as demanded by the magnetostatic theorem. The decay of this CS is responsible for the post quasi-steady rise in kinetic energy, marking onset of the third phase.

The corresponding dynamics of MFLs in the third phase is documented in Figure 11 for time instances $t = 30s$, $t = 40s$, $t = 50s$, and $t = 55s$. Noticeably, the reconnection at the extended CS reduces the pressure beneath the flux-rope because of a localized decrease in magnetic field strength. The neighboring field lines are stretched into this pressure depleted region, from all sides, rendering the rope to be dipped at the bottom portion. This dip corresponds to the observed dipped portion of a prominence, where the mass of

the prominence is believed to be situated (Ballegooijen & Cranmer 2010). Along with the stretched field lines located below the pressure depleted region, the dipped portion of the rope generates a new X-type null—denoted by X3 in the figure. Along with the rope, this new X-type null also moves upward. Further evolved, the MFLs constituting the flux-rope reconnect and the rope loses its well defined structure.

Noteworthy is importance of the translational symmetry in identifying the detached magnetic structure with a flux-rope—which is first and foremost a magnetic flux surface by its mathematical definition. Toward recognizing the importance, projection of a helical field line constituting the detached structure (Figure 6) on a y-constant surface is a closed curve. Because of the symmetry, a translation of this closed curve along y generates a surface on which the helical field lines are also tangential; confirming the detached structure to be a magnetic flux surface. In absence of the symmetry, the identification is not straightforward as field lines are always postprocessed and the processing error contributes to the topology of the obtained MFLs. Conventionally, however, the magnetostatic theorem applies to three dimensional fields, which favors the actual evolution of solar magnetized plasma. To consolidate the simulation results further, in the following we present two auxiliary computations where the symmetry is removed. The three dimensional simulations are performed on a grid of size $128 \times 128 \times 256$, resolving the same computational domain as in the symmetric case. The boundary conditions along x and y are periodic, and open in z. For consistency, all other parameters are kept identical to the symmetric case.

3.1. Auxiliary simulation I

For the first simulation, the initial magnetic field $\mathbf{B}^\star$ (Appendix B) is constructed by superposing a three dimensional solenoidal field on the $\mathbf{B}$ expressed in equations (10)-(12). Notable is the structural similarity of the two superposed fields that individually

reduce to a linear force free field for $s_0 = 1$. The evolution for this 3D simulation is shown in Figures 12 and 13. Figure 12 displays the time series for two sets of field lines, where panel a corresponds to the initial field $\mathbf{B}^{\star}$. The PIL is curved, thus attesting to the absence of translational symmetry along the y. The figure is overlaid with contours of magnetic pressure drawn on a y-constant plane. Similar to evolution depicted in Figure 7, repeated reconnections generate a detached magnetic structure which, based on the 2.5D computation, can be identified to a flux-rope. The Figure 13 illustrates the evolution with more densely plotted field lines where panel a corresponds to the initial field $\mathbf{B}^{\star}$ (corresponding animation is provided as supplementary material). The field lines constituting the rope are marked in red, and with an ascent maintained by underlying reconnections document an evolution with overall similarity to its 2.5D counterpart.

3.2. Auxiliary simulation II

For the second simulation, the initial field $\mathbf{B}^{\star\star}$ (Appendix C) is derived by superposing the $\mathbf{B}^{\star}$ with another solenoidal field $\mathbf{B}'_p$ where the $\mathbf{B}'_p$ reduces to potential field for $s_0 = 1$. In Figure 14 we illustrate the evolution of magnetic field lines (corresponding animation is provided as supplementary material). Panel a depicts the initial field lines of $\mathbf{B}^{\star\star}$ having a curved PIL. The figure confirms the formation of flux rope (marked in red) and its ascent by repetitive reconnections similar to the first 3D simulation (Figure 13). The figure is overplotted with contours of $\mid \mathbf{B}^{\star\star} \mid$ in y-constant plane and isosurfaces of corresponding current density $\mathbf{J}^{\star\star}$ with isovalues 15% and 20% of maximum $\mid \mathbf{J}^{\star\star} \mid$. Based on their appearances, the isosurfaces can be classified into two distinct categories: the surfaces appearing at the z-constant plane below the rope (marked by A in panel d) and the elongated surfaces located at horizontal sides of the rope (marked by B in panel d). The figure identifies generation of the elongated surfaces to an increase in the local number

density of parallel field lines, resulting in an increase in $\mid \mathbf{B}^{\star\star} \mid$ and hence $\mid \mathbf{J}^{\star\star} \mid$ without any sharpening of field gradient. Hence, these surfaces do not represent current sheets (Kumar et al. 2015b). In contrast, the surfaces lying in z-constant plane originate without a co-located enhancement in $\mid \mathbf{B}^{\star\star} \mid$, suggesting the development of these surfaces by a local increase in the field gradient. Thus, the appearances of these surfaces indicate the formation of current sheets below the rope (Kumar et al. 2015b). Importantly, the current sheet has a non-uniform intensity distribution along the rope, where patches of intense currents are marked in black while low currents are marked in yellow; which agrees with the general expectation. The same non-uniformity of developing CSs was also observed in the Auxiliary simulation I (not shown) which further validates the general expectation.

With the ascending flux ropes having underlying reconnections in agreement with the standard flare model (Shibata & Magara 2011), the reported simulations identify spontaneous repeated MRs as the initial driver for the rope formation and triggering its ascent. Further, the simulations underline that MRs play an active role in the feedback mechanism between flux-rope dynamics and reconnections, central to the standard flare model. This is in harmony with contemporary observations (Temmer et al. 2008, 2010; Cho et al. 2009; Cheng et al. 2011).

4. Summary and conclusions

The presented simulations start from a select motionless state with magnetic field congruent to a gauge-invariant form of linear force-free field having translational symmetry. These simulations identify repeated magnetic reconnections as an autonomous mechanism for creating a flux-rope from initially bipolar field lines and, subsequently, for triggering and maintaining its ascent via reconnections that occur below the rope. The computations being commensurate with the requirements of magnetostatic theorem, the reconnections

are spontaneous and inherent to the evolving fluid. The computational commensuration with the Parker's theorem is achieved by viscous relaxation of an incompressible, thermally homogeneous high-S magnetofluid maintaining the condition of flux-freezing. During the relaxation, sharpening of magnetic field gradient is unbounded, ultimately leading to MRs at locations where separation of non-parallel field lines approaches grid resolution. The MR process per se is underresolved, but effectively regularized by locally adaptive dissipation of MPDATA, in the spirit of ILES subgrid-scale turbulence models. In effect, the post-reconnection condition of flux-freezing is restored, and field lines tied to the reconnection outflow push other sets of MFLs, leading to secondary MRs. The whole process is replicated in time to realize repetitive reconnections.

The simulated relaxation process comprises three distinct phases. In the first phase, a combination of incompressibility and the initial Lorentz force deforms initial field lines such that the field gradient sharpens in a direction implied by the initial condition (herein x). Further push eventuates in reconnection and development of a X-type neutral point along with a detached flux-rope. Repeated reconnections around the X-type null generate more detached field lines which contribute to the rope. Moreover, being frozen to the outflow, the rope ascends vertically. Because the reconnections are localized below the evolving rope, the scenario is in general agreement with observations. As the magnetofluid relaxes to a quasi-steady state, the process enters the second phase of the relaxation with the X-type null being squashed to generate two Y-type nulls along with an extended CS beneath the rope. In the third phase the extended CS decay, resulting in an increase in the kinetic energy of mass flow. Because of the corresponding decrease in magnetic intensity near the decaying CS, MFLs from all side of the CS are stretched into the field depleted region. The rope becomes dipped at the bottom and a new X-type null is generated which ascends with the rope. Continued further in time, the flux-rope reconnects internally and loses its structure. Fully three dimensional simulations are also performed to verify the robustness

of repeated spontaneous MRs in creation and ascent of a rope accordant to a more realistic evolution. Importantly, the three dimensional simulations document the intensity of CSs developed over respective PILs to be non-uniform—a feature expected in realistic ropes developed via reconnections.

Altogether the computations extend Parker's magnetostatic theorem to the scenario of evolving magnetic fields which can undergo magnetic reconnection. Notably, the theorem in absence of magnetic diffusivity leads to CSs, having true mathematical singularities in magnetic field which are end states of any evolution. But in presence of small but non-zero magnetic diffusivity, as in astrophysical plasmas, the theorem opens up the possibility of spontaneous generation of secondary CSs and subsequent MRs that may contribute to the dynamics of the plasma. The computations confirm the contribution to be meaningful as it can generate observed magnetic structures and govern their dynamics which, in this case, is the evolution of a flux-rope in terms of its generation and ascent in a magnetic topology relevant to the solar corona. Additionally, in context of the standard flare model, the simulations imply a direct involvement of magnetic reconnection in the activation of flux-ropes.

Acknowledgements: The simulations are performed using the 100 TF cluster Vikram-100 at Physical Research Laboratory, India. One of us (PKS) is supported by funding received from the European Research Council under the European Union's Seventh Framework Programme (FP7/2012/ERC Grant agreement no. 320375). The authors also sincerely thank an anonymous reviewer for providing specific suggestions to enhance the presentation as well as to raise the academic content of the paper.

A. Appendix

To solve a linear force-free equation, the magnetic field is identified as a Chandrasekhar-Kendall (Chandrasekhar & Kendall 1957) eigenfunction which, in Cartesian coordinate can be written as

$$\mathbf{Y} = \nabla \times \psi \hat{e_y} + \frac{1}{\alpha_0} \nabla \times (\nabla \times \psi \hat{e_y}) \quad , \tag{A1}$$

where $\psi = \psi(x, y, z)$ is a scalar function and α_0 is constant. Substitution of $\mathbf{Y}$ in the linear force-free equation gives,

$$\nabla \times (\nabla \times \nabla \times \psi \hat{e_y} - {\alpha_0}^2 \psi \hat{e_y}) = 0 \quad , \tag{A2}$$

implying,

$$(\nabla \times \nabla \times \psi \hat{e_y} - {\alpha_0}^2 \psi \hat{e_y}) = \nabla \lambda \quad , \tag{A3}$$

where the scalar function $\lambda = \lambda(x, y, z)$ represents an arbitrary gauge. Using the identity

$$\nabla \times \nabla \times \psi \hat{e_y} = -\nabla^2 \psi \hat{e_y} + \nabla(\nabla \cdot \psi \hat{e_y}) \quad , \tag{A4}$$

results in the inhomogeneous vector Helmholtz equation for the magnetic field

$$(\nabla^2 \psi + {\alpha_0}^2 \psi) \hat{e_y} = \nabla(\nabla \cdot \psi \hat{e_y} - \lambda) \quad . \tag{A5}$$

Standardly, a three dimensional analytical solution of the linear force-free equation is obtained by only solving the homogeneous equation which corresponds to the selection of

$$\lambda = \nabla \cdot \psi \hat{e_y} \ , \tag{A6}$$

for the gauge. If $\partial / \partial y \equiv 0$, the solution for the linear force-free equation is gauge independent, and the scalar function ψ satisfies Helmholtz equation

$$\nabla^2 \psi + \alpha_0^2 \psi = 0 \quad . \tag{A7}$$

Consequently, for a geometry relevant to solar corona, the field components are

$$B_{\mathrm{lf}\,x} = k_z \sin(k_x x) \exp\left(-k_z z\right), \tag{A8}$$

$$B_{\mathrm{lf}\,y} = \sqrt{{k_x}^2 - {k_z}^2} \sin(k_x x) \exp\left(-k_z z\right), \tag{A9}$$

$$B_{\mathrm{lf}\,z} = k_x \cos(k_x x) \exp\left(-k_z z\right), \tag{A10}$$

with $\alpha_0 = \sqrt{{k_x}^2 - {k_z}^2}$.

B. Appendix

A three dimensional linear force-free field $\mathbf{B}'_{lf}$, with the choice of gauge, has components

$$B'_{lf\,x} = \alpha_0 l_y \sin(l_x x) \cos(l_y y) \exp\left(-l_z z\right) - l_x l_z \cos(l_x x) \sin(l_y y) \exp\left(-l_z z\right), \tag{B1}$$

$$B'_{lf\,y} = -\alpha_0 l_x \cos(l_x x) \sin(l_y y) \exp\left(-l_z z\right) - l_y l_z \sin(l_x x) \cos(l_y y) \exp\left(-l_z z\right), \tag{B2}$$

$$B'_{lf\,z} = ({l_x}^2 + {l_y}^2) \sin(l_x x) \sin(l_y y) \exp\left(-l_z z\right), \tag{B3}$$

with $\alpha_0 = \sqrt{{l_x}^2 + {l_y}^2 - {l_z}^2}$. The three dimensional simulation is performed with an initial field

$$\mathbf{B}^\star = \mathbf{B} + a_0 \mathbf{B}' \tag{B4}$$

for $a_0 = .5$ and $\mathbf{B}'$ having components

$$B'_x = \sin(x)\cos(y) \exp\left(-\frac{z}{s_0}\right) - \cos(x)\sin(y) \exp\left(-\frac{z}{s_0}\right), \tag{B5}$$

$$B'_y = -\cos(x)\sin(y) \exp\left(-\frac{z}{s_0}\right) - \sin(x)\cos(y) \exp\left(-\frac{z}{s_0}\right), \tag{B6}$$

$$B'_z = 2 s_0 \sin(x)\sin(y) \exp\left(-\frac{z}{s_0}\right). \tag{B7}$$

C. Appendix

The force-free field $\mathbf{B}_{\rm lf}$ (Appendix A) reduces to a two-dimensional potential field $\mathbf{B}_p$ with $k_x = k_z = k$. Then, the components of the $\mathbf{B}_p$ are

$$B_{p_x} = k \sin(kx) \exp(-kz), \tag{C1}$$

$$B_{p_y} = 0, \tag{C2}$$

$$B_{p_z} = k \cos(kx) \exp(-kz), \tag{C3}$$

with $\alpha_0 = 0$. The additional three dimensional simulation is conducted with the initial field

$$\mathbf{B}^{\star\star} = \mathbf{B}^{\star} + \mathbf{B}'_p \tag{C4}$$

where $\mathbf{B}'_p$ (derived from the $\mathbf{B}_p$) has the components

$$B_{p_x}{}' = \sin(x) \exp\left(-\frac{z}{s_0}\right), \tag{C5}$$

$$B_{p_y}{}' = 0, \tag{C6}$$

$$B_{p_z}{}' = s_0 \cos(x) \exp\left(-\frac{z}{s_0}\right). \tag{C7}$$

REFERENCES

Amari, T., Luciani, J. F., Mikic, Z., & Linker, J. 1999, ApJ, 518, L57

Amari, T., Luciani, J. F., Aly, J. J., Mikic, Z., & Linker, J. 2003, ApJ, 585, 1073

Aschwanden, M. J. 2004, *Physics of the Solar Corona* (Springer, Berlin)

Aulanier, G., Pariat, E., & Démoulin, P. 2005, A&A, 444, 961

Aulanier, G., Török, T., Démoulin, P., & DeLuca, E. E. 2010, ApJ, 708, 314

Beaudoin, P., Charbonneau, P., Racine, E., & Smolarkiewicz, P. K. 2013, Sol. Phys., 282, 335

Bhattacharyya, R., Low, B. C., & Smolarkiewicz, P. K. 2010, Phys. Plasmas, 17, 112901

Chandrasekhar, S., & Kendall, P. C. 1957, ApJ, 126, 457

Chatterjee, P., & Fan, Y. 2013, ApJ, 778, L8

Cheng, X., Zhang, J., Liu, Y., & Ding, M. D. 2011, ApJ, 732, L25

Cho, K., -S., Lee, J., Bong, S. -C., Kim, Y. -H., Joshi, B., & Park, Y. -D. 2009, ApJ, 703, 1

Choe, G. S., & Lee, L. C. 1996, ApJ, 472, 372

Clyne, J., & Rast, M. 2005, in *Visualization and Data Analysis* (ed. R. F. Erbacher, J. C. Roberts, M. T. Gordon & K. Borner), pp. 284-294, SPIE

Dahlburg, R. B., Antiochos, S. K., & Zang, T. A. 1991, ApJ, 383, 420

DeVore, C. R., & Antiochos, S. K. 2000, ApJ, 539, 954

Domaradzki, A., Xiao, Z., & Smolarkiewicz, P. K. 2003, Phys. Fluids, 15, 3890

Fan, Y. 2001, ApJ, 554, L111

Fan, Y., & Gibson, S. E. 2003, ApJ, 589, L105

Fan, Y. 2010, ApJ, 719, 728

Fan, Y. 2011, ApJ, 740, 68

Fan, Y. 2016, arXiv:1604.05687v1

Ghizaru, M., Charbonneau, P., & Smolarkiewicz, P. K. 2010, ApJ, 715, L133

Grinstein, F. F., Morgolin, L. G., & Rider, W. J. 2007, *Implicit Large Eddy Simulation: Computing Turbulent Fluid Dynamics* (Cambridge University Press)

Joshi, B., Kushwaha, U., Cho, K., -S., & Veronig, A. M. 2013, ApJ, 771, 1

Krucker, S., Battaglia, M., Cargill, P. J., Fletcher, L., Hudson, H. S., MacKinnon, A. L., Masuda, S., Sui, L., Tomczak, M., Veronig, A. L., Vlahos, L., & White, S. M. 2008, A&A Rev., 16, 155

Kumar, D., Bhattacharyya, R., & Smolarkiewicz, P. K. 2013, Phys. Plasmas, 20, 112903

Kumar, D., Bhattacharyya, R., & Smolarkiewicz, P. K. 2015a, Phys. Plasmas, 22, 012902

Kumar, S., Bhattacharyya R., & Smolarkiewicz, P. K. 2014, Phys. Plasmas, 21, 052904

Kumar, S., Bhattacharyya R., & Smolarkiewicz, P. K. 2015b, Phys. Plasmas, 22, 082903

Kusano, K., Suzuki, Y., Kubo, H., Miyoshi, T., & Nishikawa, K. 1994, ApJ, 433, 361

Kushwaha, U., Joshi, B., Veronig, A. M., & Moon, Y., -J. 2015, ApJ, 807, 101

Margolin, L. G., Rider, W. J., & Grinstein, F. F. 2006, J. Turbul., 7, N15

Parker, E. N. 1972, ApJ, 174, 499

Parker, E. N. 1988, ApJ, 330, 474

Parker, E. N. 1994, *Spontaneous Current Sheets Formation in Magnetic Fields* (Oxford University Press, New York)

Parker, E. N. 2012, Plasma Phys. Control. Fusion, 54, 124028

Priest, E. R. 1982, *Solar Magnetohydrodynamics* (Reidel, Dordrecht)

Prusa, J. M., Smolarkiewicz, P. K., & Wyszogrodzki, A. A. 2008, Comput. Fluids, 37, 1193

Ruderman, M. S., & Roberts, B. 2002, ApJ, 577, 475

Shibata, K., & Magara, T. 2011, Living Rev. Solar Phys., 8, lrsp-2011-6

Smolarkiewicz, P. K. 2006, Int. J. Numer. Methods Fluids, 50, 1123

Smolarkiewicz, P. K., & Charbonneau, P. 2013, J. Comput. Phys., 236, 608

Temmer, M., Veronig, A. M., Vršnak, B., Rybák, J., Gömöry, P., Stoiser, S., & Maričić, D. 2008, ApJ, 673, L95

Temmer, M., Veronig, A. M., Kontar, E. P., Krucker, S., & Vršnak, B. 2010, ApJ, 712, 1410

van Ballegooijen, A. A., & Martens, P. C. H. 1989, ApJ, 343, 971

van Ballegooijen, A. A., & Cranmer, S. R. 2010, ApJ, 711, 164

Xia, C., Keppens, R., & Guo, Y. 2014, ApJ, 780, 130

This manuscript was prepared with the AAS LaTeX macros v5.2.

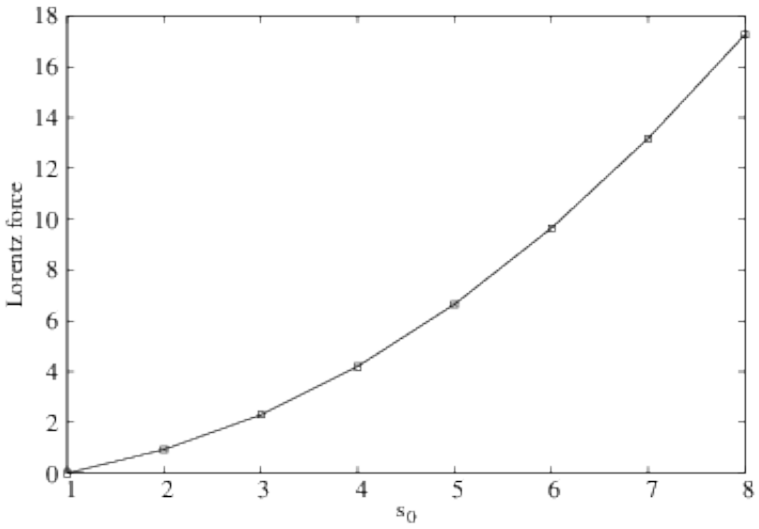

Fig. 1.— Variation of $\mid \mathbf{J} \times \mathbf{B} \mid_{\max}$ with an increase in s_0. The plots show a monotonous increase in Lorentz force with an increase in s_0.

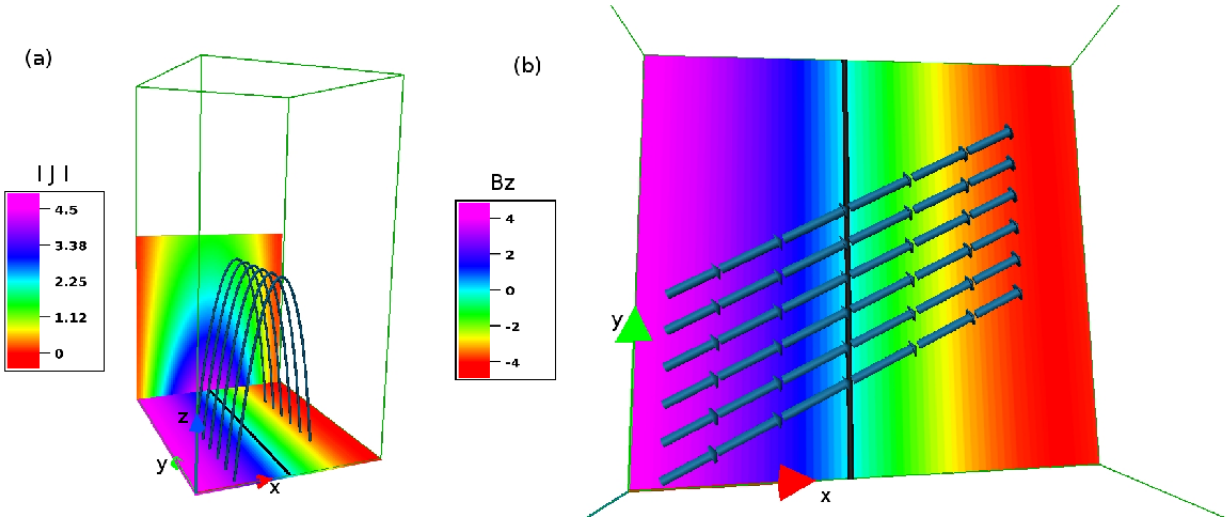

Fig. 2.— The panel a and b illustrate magnetic field lines of the initial field $\mathbf{B}$ for $s_0 = 6$ and their projections of the $z = 0$ plane respectively. The projected field lines are inclined to the x-axis with an angle ϕ, manifesting the sheared nature of MFLs. Both panels are overlaid with contours of the z-component of $\mathbf{B}$ (B_z) on the $z = 0$ plane along with straight PIL (in color black), indicating polarities of footpoints. Additionally, in panel a, contours of magnitude of current density ($\mid \mathbf{J} \mid$) are plotted on a y-constant plane to depict the current density inside the sheared arcades.

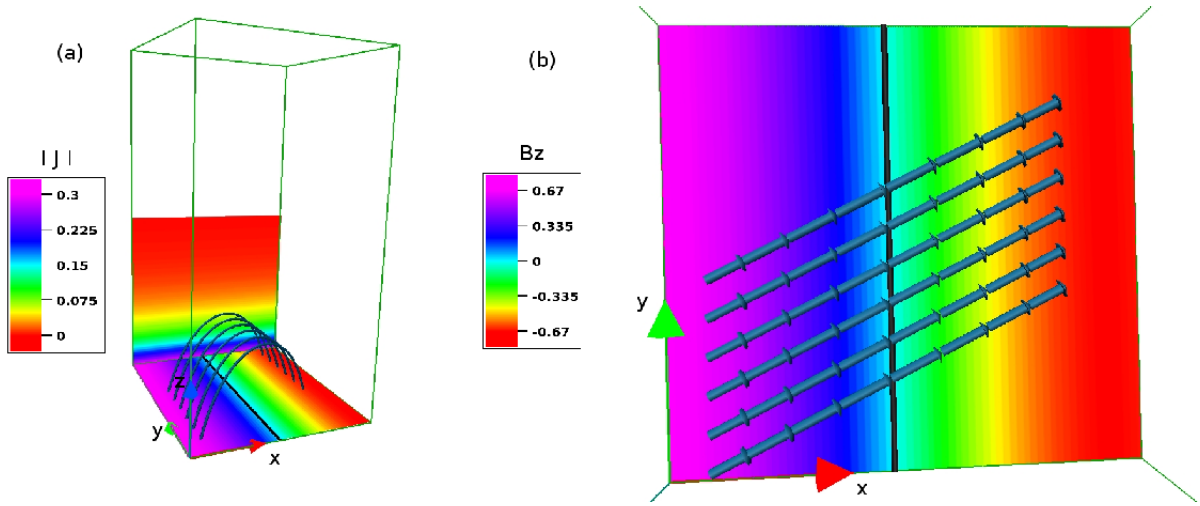

Fig. 3.— As in Fig. 2 but for field lines of $\mathbf{B}_{\rm lf}$ and their projections on the $z = 0$ plane. The figure demonstrates the morphology and shear of the initial field $\mathbf{B}$ to be identical to the corresponding $\mathbf{B}_{\rm lf}$ characterized by $s_0 = 1$.

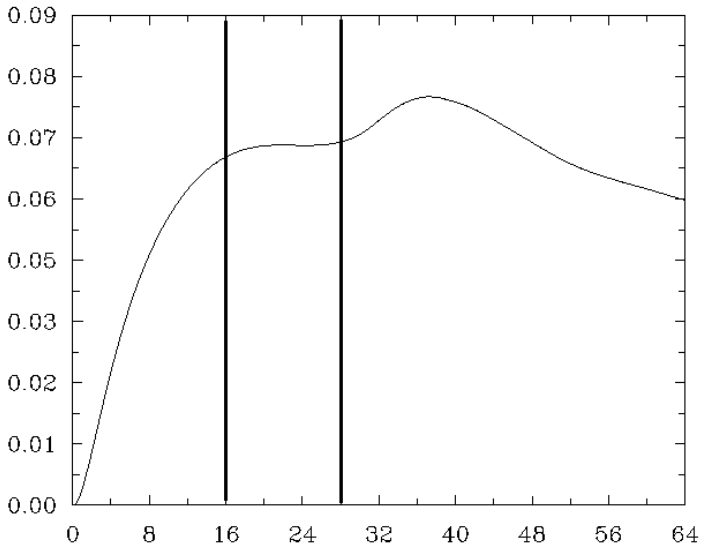

Fig. 4.— The evolution of kinetic energy, normalized to initial total (kinetic+magnetic) energy. Noteworthy are the three distinct phases of the evolution, marked by vertical lines in the plot.

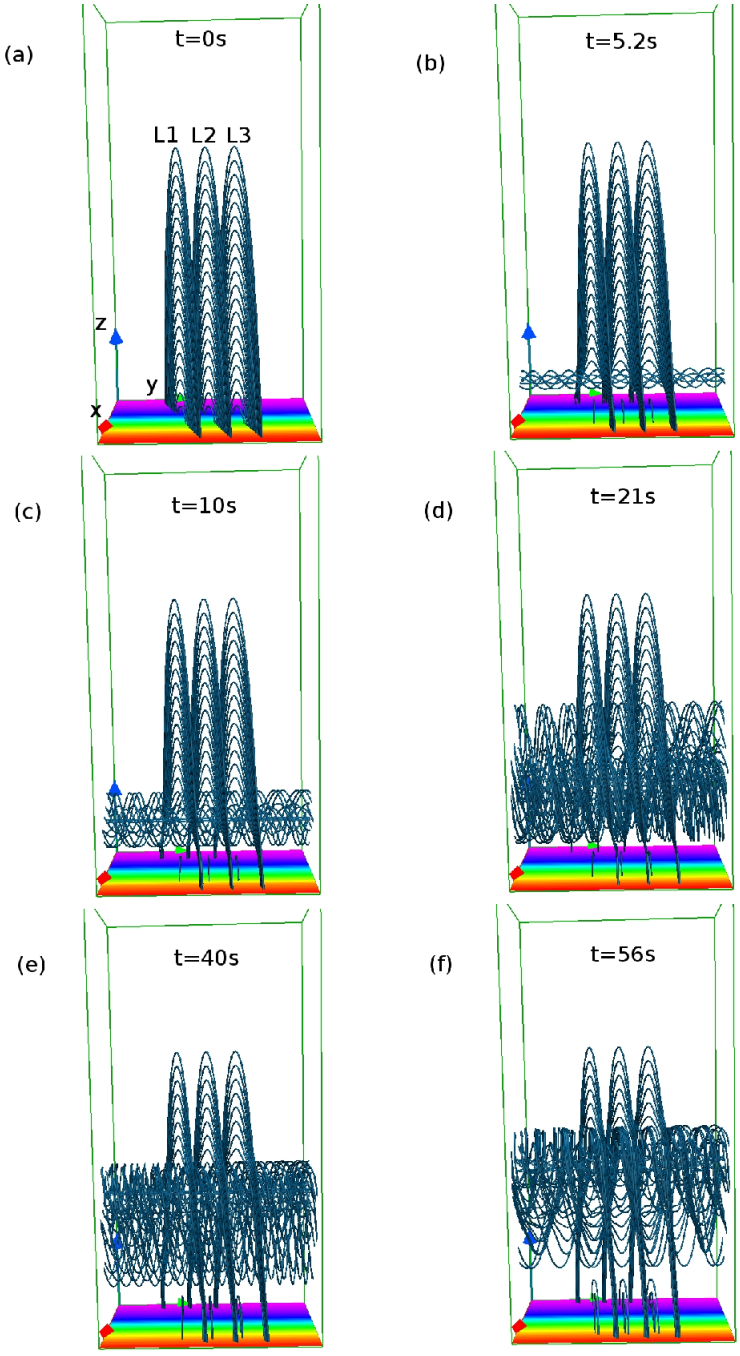

Fig. 5.— Time sequences of magnetic field lines in their important phases of evolution. Three different sets of magnetic loops are sketched, denoted by L_1, L_2 and L_3 in panel a of the figure. Important is formation of detached magnetic structure resembling a magnetic flux-rope. Also evident is the ascend of this structure while being situated over the PIL.

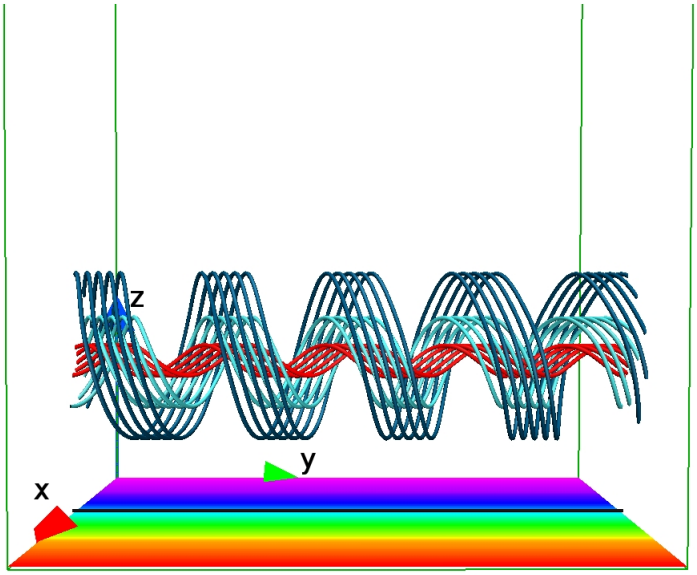

Fig. 6.— Snapshot of field lines at $t = 10s$, plotted in the neighborhood of the detached structure. The figure verifies the detached magnetic structure to be comprised of a stack of co-axial cylindrical magnetic flux surfaces which are made of helical field lines.

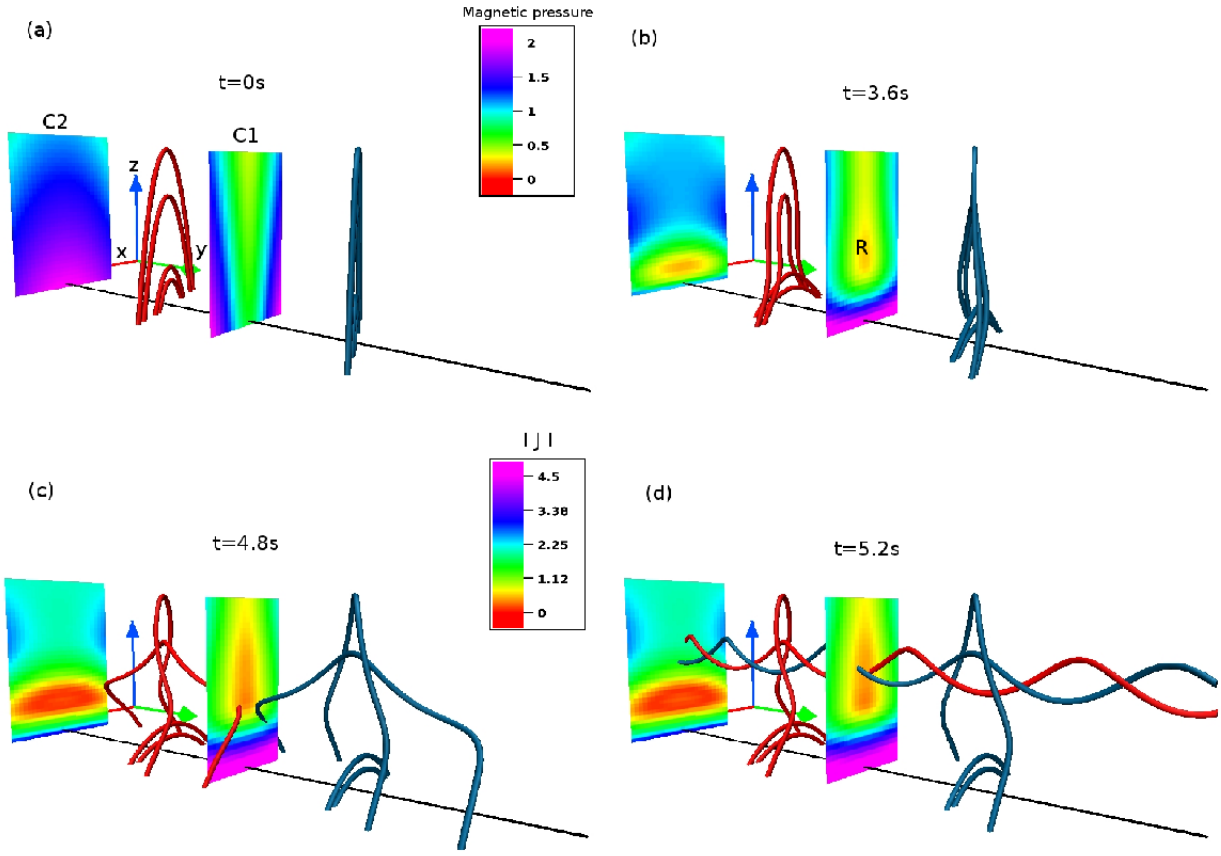

Fig. 7.— Evolution of magnetic field lines concurrent with the first phase. The figure is overlaid with contours of magnetic pressure (marked by C1 in panel a) and magnitude of current density (marked by C2 in panel a) drawn on different y-constant planes. The PIL is the solid black line. Panel b documents the implosion of MFLs situated at lower height along with an increase in their footpoint separation which results in depletion of magnetic pressure (symbolized by R) in the y-constant plane. Parts of MFLs are dragged into this pressure depleted region R from both sides of PIL, which sharpens up the gradient in $\mathbf{B}$ (panel c). Subsequent reconnection leads to the generation of detached helical field lines (panel d). The current contours confirm the absence of an extended CS.

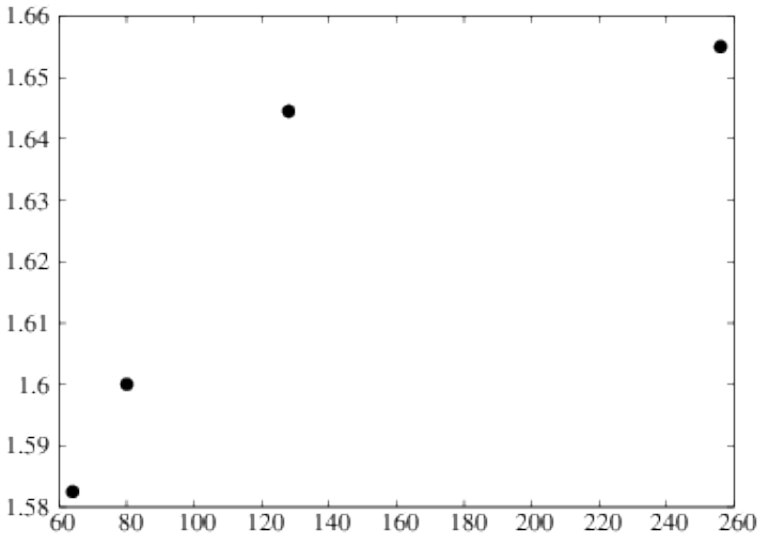

Fig. 8.— The plot of current density (in vicinity of R as marked in panel b of Fig. 7) against grid resolution. The abscissa is grid resolution along z whereas the ordinate is current density. The monotonous increase of current density with resolution asserts the increase of gradient in magnetic field.

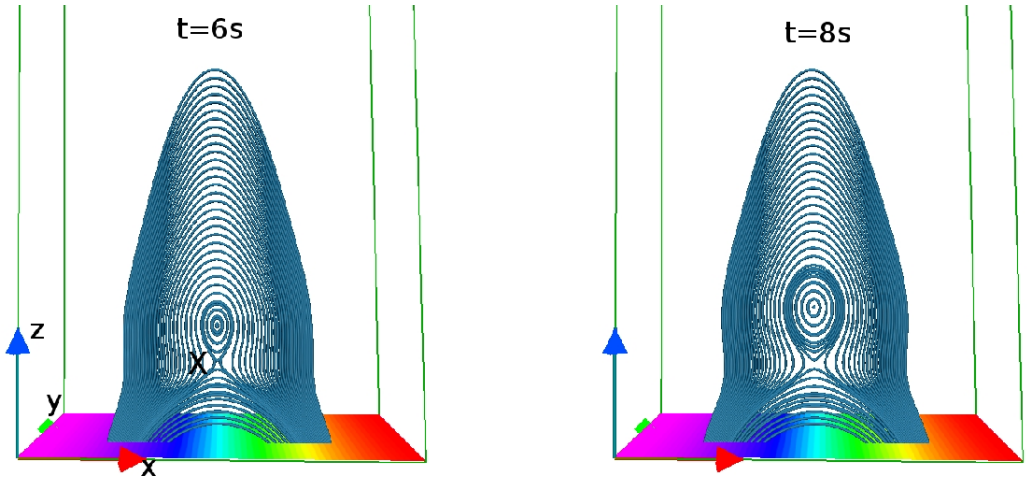

Fig. 9.— Time sequence of field lines at instances $t = 6s$ and $t = 8s$, projected on a y-constant plane. Panel a documents the presence of a magnetic island, reminiscent of the rope, along with a X-type null (marked by the symbol X) below the island. The panel b shows the number of field lines constituting the island increases while the center rises along the vertical.

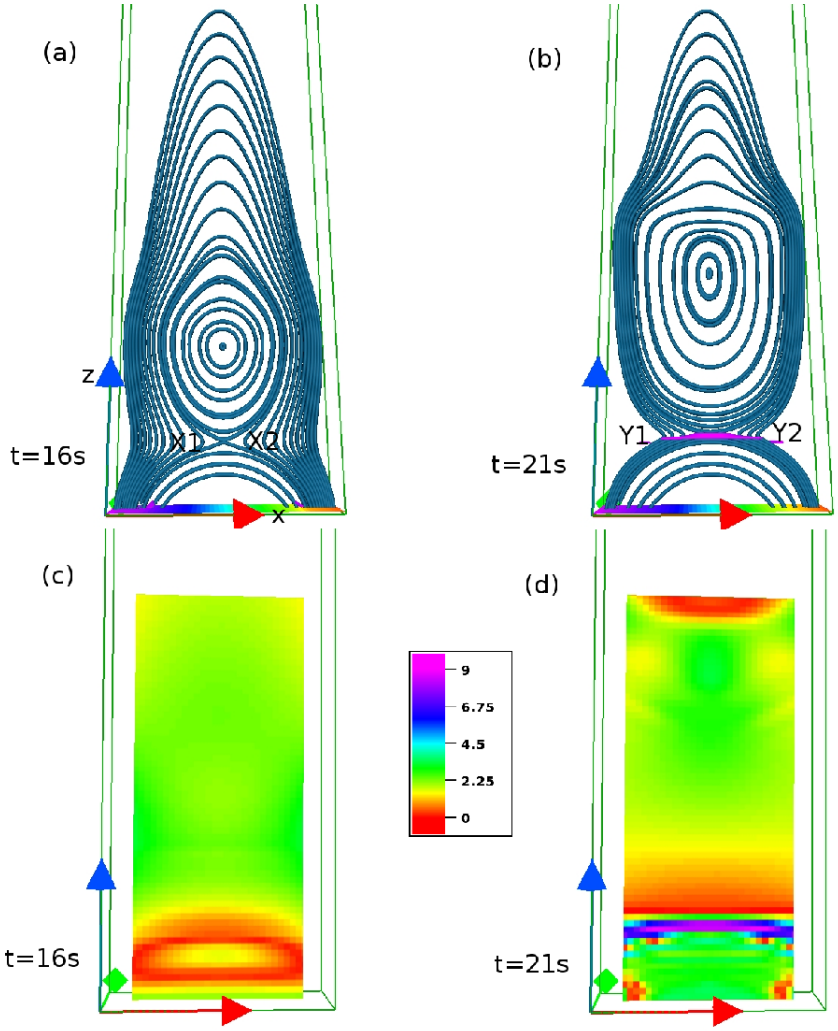

Fig. 10.— Evolution of field lines (projected on a y-constant plane) coincides with quasi-steady state of the relaxation (panels a and b). In addition, the contours of magnitude of current density the y-constant plane are plotted in panels c and d. Noteworthy are the pressing of two quadrants (shown by symbols X1 and X2 in panel a) and generation of two Y-type nulls (denoted by symbols Y1 and Y2 in panel b) along with an extended CS (depicted in color pink in panel b). The development of extended CS is also attested by the current contours in panel d.

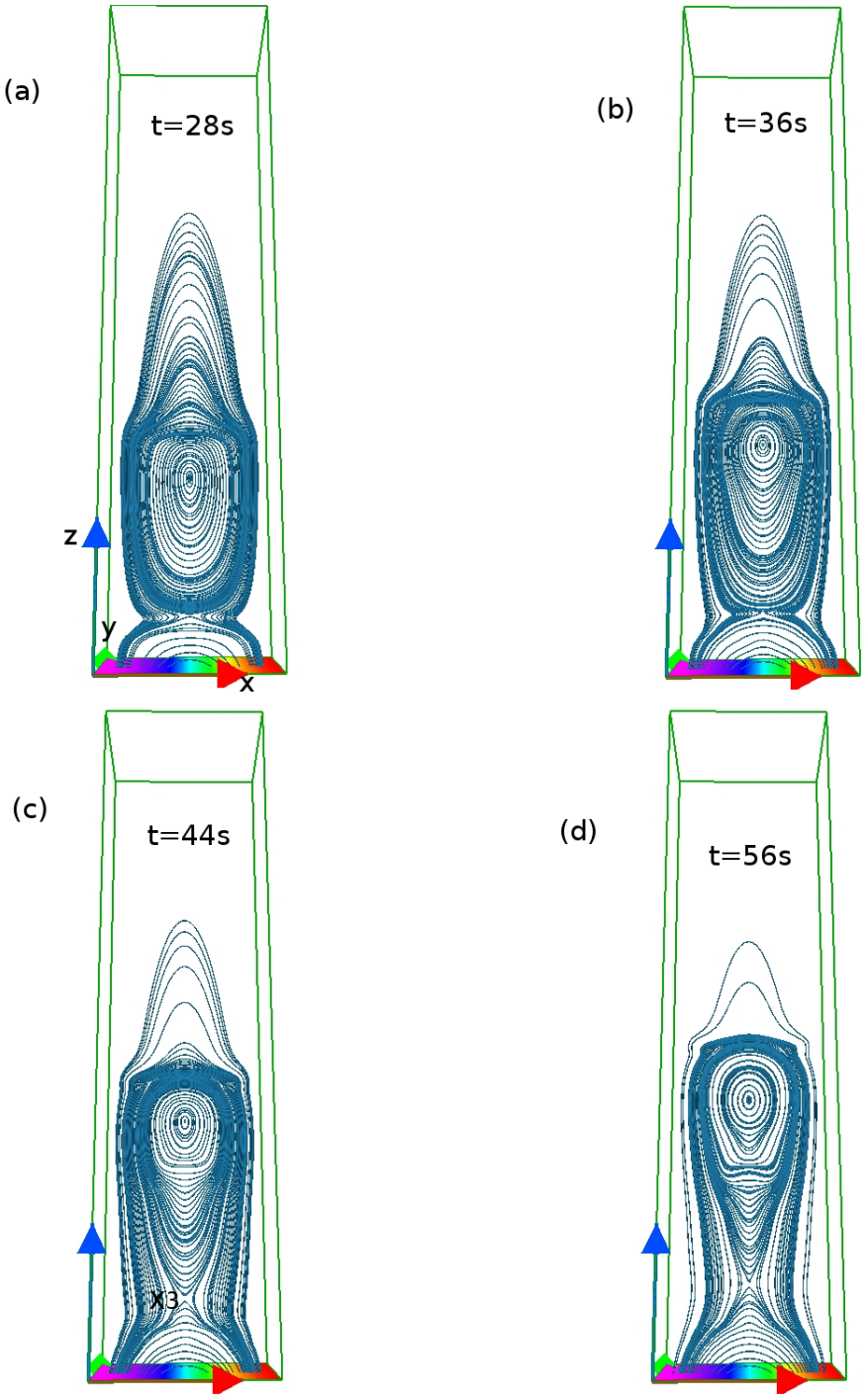

Fig. 11.— The figure plots field lines during the third phase of evolution. The field lines are projected on a y-constant plane. Important is the onset of a new X-type null (illustrated by $X3$) while the bottom portion of the rope develops a dip (panel c). Also, the newly formed X-point moves upward along with the rope (panel d).

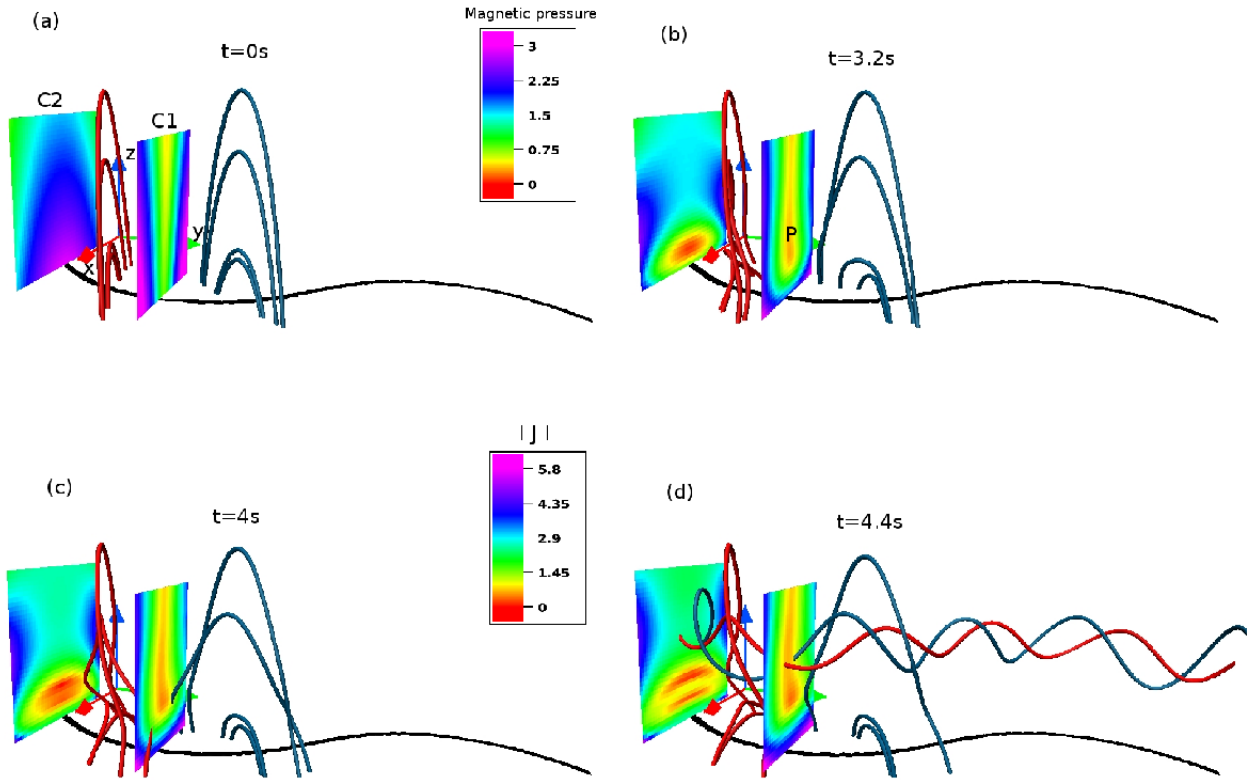

Fig. 12.— Time sequences of two sets of field lines for the three dimensional simulation with initial field $\mathbf{B}^{\star}$. The panel a shows the field lines of the initial field. Important to note is the curved PIL (the solid black line). The figure is further overlaid with contours of magnetic pressure (denoted by C1 in panel a) and current density (denoted by C2 in panel a) plotted on different y-constant planes. Panels b, c and d document the development of magnetic pressure depleted region (symbolized by P) in the y-constant plane and subsequent reconnection which leads to the generation of a flux-rope. Also, the flux-rope is situated above the PIL. Moreover, the current contours depict that no extended CS originates during this phase of the evolution.

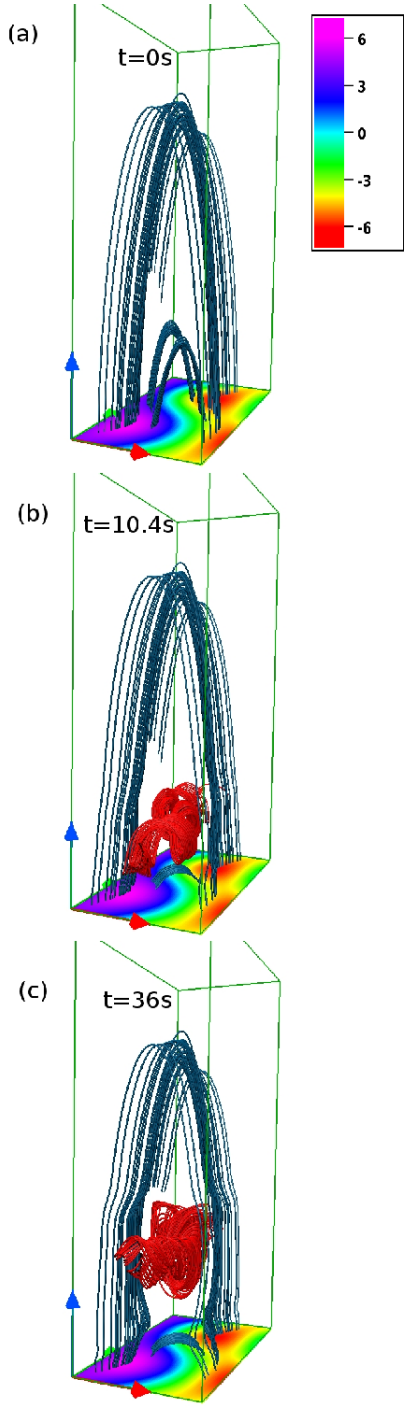

Fig. 13.— Time sequences of evolution with more densely plotted field lines of the $\mathbf{B}^{\star}$. The lines in red marks the flux-rope. The overall evolution is similar to the 2.5D case. Noticeable is the ascend of the rope. The animated evolution is presented as supplementary material.

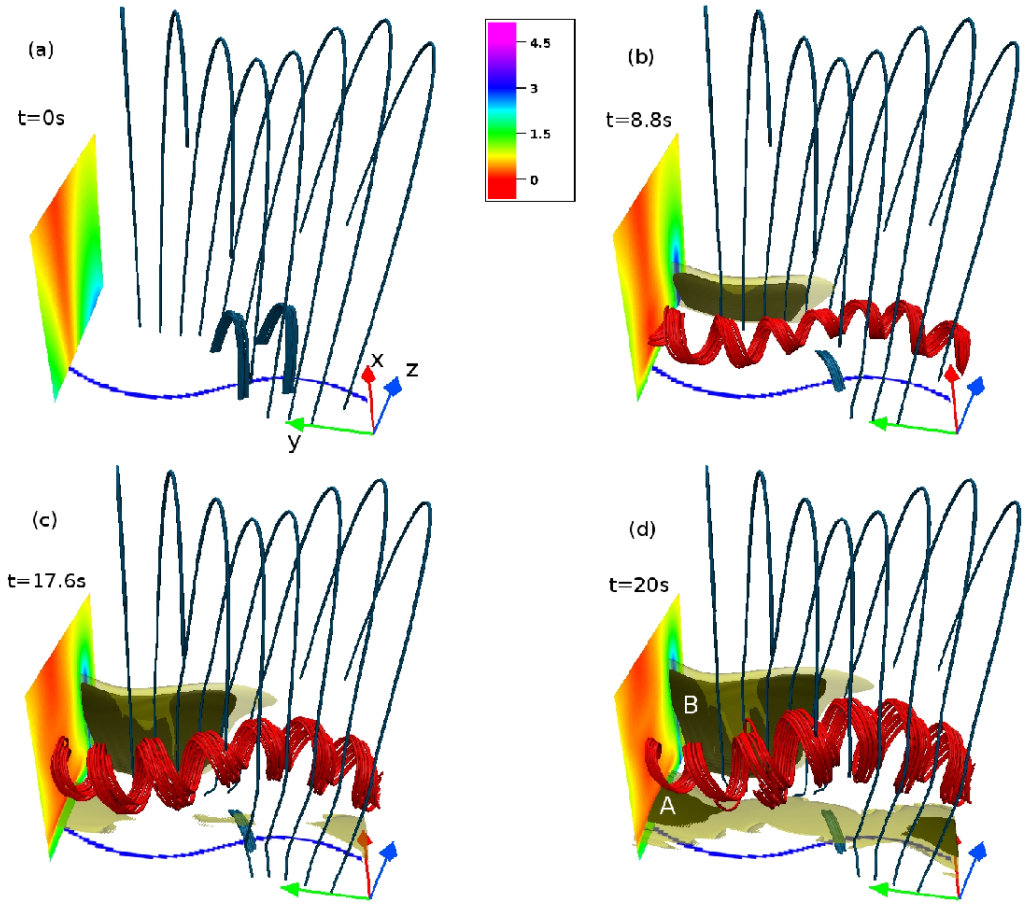

Fig. 14.— Evolution of field lines for the three dimensional simulation with initial field $\mathbf{B}^{\star\star}$, illustrated in panel a (the curved PIL is shown by the solid blue line). The figure is further overlaid with isosurfaces of current density with isovalues 15% (in color yellow) and 20% (in color black) of its maximum and contours of $\mid \mathbf{B}^{\star\star} \mid$ on a y-constant plane. The helical red field lines identify the flux-rope which rises in the vertical direction. Notable is the development of current sheet below the rope (marked by A in panel d). The elongated surfaces (marked by B in panel d) being co-located with enhanced $\mid \mathbf{B}^{\star\star} \mid$ region in y-constant plane imply that their onset does not indicate CS formation. The animated evolution is presented as supplementary material.